

Modeling for Ultrasonic Health Monitoring of Foams with Embedded Sensors

Interim Progress Report

15 March 02 --- 13 March 05

L. Wang and S. I. Rokhlin

The Ohio State University
Nondestructive Evaluation Program
Department of Industrial, Welding and Systems Engineering
1248 Arthur E. Adams Drive

Columbus, OH 43221

Principal Investigator:

Professor Stanislav I. Rokhlin
Tel.: (614) 292-7823, Fax: (614)292-3395
e-mail: rokhlin.2@osu.edu

Abstract

In this report analytical and numerical methods are proposed to estimate the effective elastic properties of regular and random open-cell foams. The methods are based on the principle of minimum energy and on structural beam models. The analytical solutions are obtained using symbolic processing software. The microstructure of the random foam is simulated using Voronoi tessellation together with a rate-dependent random close-packing algorithm. The statistics of the geometrical properties of random foams corresponding to different packing fractions have been studied. The effects of the packing fraction on elastic properties of the foams have been investigated by decomposing the compliance into bending and axial compliance components. It is shown that the bending compliance increases and the axial compliance decreases when the packing fraction increases.

Keywords: Foam; Elastic properties; Finite element; Randomness

1. Introduction

Structural foams are made with high stiffness-to-weight ratio and high-energy absorption and are very suitable for lightweight structures and insulating materials [1-4]. Different materials can be foamed by a variety of manufacturing processes. For example, metals can be foamed by injecting gases or by adding gas-releasing blowing agents [1]. The foams produced exhibit different microstructures and may have open and closed cells with different degrees of randomness.

Foams are highly heterogeneous materials with mechanical and acoustic properties determined not only by the frame material but also to a significant degree by their microstructure. To model the properties of these materials, one first needs to generate the microstructures. The actual foam microstructure can be obtained by 3-D X-ray tomography [5]. The microstructures can also be simulated. In analysis, foams are often approximately represented as a periodic array of regular cells such as hexagonal and truncated octahedron. The random foams may also be simulated with Voronoi tessellation [6-10]. In this approach the randomness of the foams is determined by the distribution of the "seed points" which are usually generated using hard spherical (disks) packing algorithms [10]. Another approach which is particularly useful in modeling bicontinuous media is the level-cut Gaussian random field scheme [10,11].

The elastic properties of the foams are closely related to their microstructures. For regular cells, by analyzing the smallest unit cell and representing each strut by a structural beam, analytical formulations were obtained for some 2-D and 3-D structures [12-17]. In these studies, the regular foams were usually assumed to be formed by cells

arranged in periodic arrays. Using thin beam or plate theories, the elastic constants (modulus and Poisson ratio) can be explicitly determined as functions of the microstructure of the cell. Using this approach, an analytic formulation for open cells with tetrakaidecahedral microstructure has been obtained [16, 17]. It has also been shown that the elastic properties for 3-D regular structures can be obtained by averaging in different directions [15] the properties obtained for 2-D structures. Empirical data shows that, for random open cell structures, the modulus is a power function of the relative density [2]. Rigorous analyses of random structures have been obtained using finite element analysis based on structural beam elements [7] and solid cubic elements [9].

In this report we describe a general approach to model the elastic properties of regular open-cell foams numerically and analytically, based on the principle of minimum energy and on structural beam models. Examples for 2-D general honeycomb, triangular and rectangular cells and 3-D orthogonal, rhombic dodecahedron and truncated octahedron are given. We found the cell compliance matrix can usually be decomposed into two terms which correspond to bending and axial compliances respectively. Also foams with different degrees of randomness have been simulated using a rate-dependent random packing algorithm and Voronoi tessellation. Then the effect of packing fraction on the elastic properties has been addressed. Here we will discuss the evolution of the geometry property of the random foams generated from the Voronoi diagram for both 2D and 3D using the rate-dependent algorithm described above. The corresponding elastic properties will be discussed in the following sections.

2. Simulation of 2D and 3D foam microstructures

In order to understand the relation between foam microstructure (distribution of cell shape, size and flaws in the cells) and elastic properties, one needs to simulate open foam microstructures with specific geometrical properties. Due to the similarity between the Voronoi diagram and foam microstructures, the Voronoi tessellation has been widely used to simulate the foam structures [6-10]. Here we will describe a procedure to generate foams with different regularities by combining a rate-dependent closed random packing algorithm with Voronoi tessellation.

2.1. Voronoi tessellations

In this simulation a random set of seed points or nuclei is first generated. Then the Voronoi tessellation algorithm is used to partition the space into cells, each of which consists of the area enclosing one particular nucleus (we have used the “Quickhull” [18] algorithm to produce Voronoi tessellation for 2D and 3D dimensions). For open-cell foams, the struts are formed by the edges of the Voronoi cells.

The regularity of the generated cells is determined by the distribution of the nuclei. For regular distributions, foams with ordered uniform cells are generated. Figures 1 and 2 show simulated regular 2-D and 3-D Voronoi cells whose elastic properties will be discussed in the following sections. Figure 1 shows the (a) rectangular, (b) triangular and (c) general hexagonal 2-D structures corresponding to rectangular, hexagonal and triangular nuclei respectively. The smallest repeating cells are shown in the bottom of the figures. Figure 2 shows 3-D structures: (a) cubic, (b) rhombic dodecahedron and (c)

truncated octahedron structures. The Voronoi unit cells are shown in the bottom of these figures.

2.2. *Random Voronoi tessellations*

The advantage of the Voronoi method is that it allows simulating microstructures with different level of randomness, which reflects the natural variations in microstructure in practical foams. The regularity of the simulated foams is determined by the randomness of the seed nuclei. There are different point-process algorithms to generate spatial points with different degrees of randomness [19]. The simple sequential inhibition and the close random packing point process can be used to produce a set of points widely varying in regularity. The Gibbs point processes are good models for structures with some degree of regularity and the Poisson point processes for random structures without regularity.

Here we use the close random packing point process to generate spatial points (seed nuclei) with different randomness. The randomness of the spatial points is represented by the packing fraction ϕ . Different computer algorithms have been proposed to achieve the maximum packing fraction ϕ_c . The maximum packing fraction ϕ_c of a rate-dependent densification algorithm [20, 21] can reach 0.649, of a Monte Carlo scheme [22] can achieve 0.68 and a “drop and roll” algorithm [23] 0.60. Because of the efficiency of the rate-dependent densification algorithm, we will apply it to generate random nuclei with different regularities and combine it with Voronoi tessellation to obtain foam structures with different regularities. In this section statistics of geometrical

characteristics of the cell are studied. The statistical description of the foam elastic properties will be discussed in the following sections.

In the rate-dependent densification algorithm [20, 21], first a set of N full random points are generated in a rectangle (2D) or cubic (3D) box with edge length B with periodic boundaries as the starting state for iteration. Each point is the center of an inner and an outer circle for 2D or sphere for 3D. At iteration step i , the diameter d_i of the inner sphere or circle is the minimum distance between any two points. The corresponding

minimum packing fraction is $\phi_i = \frac{\pi N}{6} \left(\frac{d_i}{B}\right)^3$ for 3D or $\phi_i = \frac{\pi N}{4} \left(\frac{d_i}{B}\right)^2$ for 2D. In each

step, the two points with minimum distance are spread apart symmetrically along the line joining their centers until the distance between these centers are equal the outer diameter D_i . Then the diameter D_i of the outer sphere or circle is reduced based on the minimum

packing fraction ϕ_i and the maximum packing fraction Φ_i ($\Phi_i = \frac{\pi N}{6} \left(\frac{D_i}{B}\right)^3$ for 3D or

$\Phi_i = \frac{\pi N}{4} \left(\frac{D_i}{B}\right)^2$ for 2D) at step i [21]

$$D_{i+1} = D_i - \frac{R}{N} (\Phi_i - \phi_i)^\alpha, \quad (1)$$

where R and α are parameters to control the convergence rate. The initial value of the

outer diameter is $D_0 = B \left(\frac{6}{\pi N}\right)^{\frac{1}{3}}$ for 3D and $D_0 = B \left(\frac{4}{\pi N}\right)^{\frac{1}{2}}$ for 2D, which results in

maximum packing fraction $\Phi_0 = 1$. Iteration continues by spreading the new pair of points with minimum distance until the inner diameter is no less than the outer diameter.

As an example, Figure 3 shows the evolution of the minimum packing fraction. For random foam simulation, in the 2D case we use 1000 nuclei points in a unit rectangle area with control parameters $R=0.00015$ and $\alpha=0.01$ and reach the final packing fraction 0.816. For 3D foams, we use 2000 nuclei points in a unit cubic volume with control parameters $R=0.0001$ and $\alpha=0.3$ and reach the final packing fraction is 0.643. Although the packing fraction is not monotonically increasing with iteration number, in general the packing fraction steadily increases and the variation amplitude decreases. The point sets corresponding to the iteration on the upper profile represent points with different packing fraction. Using the point sets obtained with different packing fraction, the corresponding Voronoi diagrams are obtained by the “Quickhull” algorithm. Examples for 2D and 3D foam structure evolutions with increase of packing fraction are shown in Figures 4 and 5. Zero packing fraction corresponds to the initial fully random state. As can be seen, as packing fraction increases, the size and shape of the cells become more uniform. Statistics of the geometrical properties of the random foams will be discussed in the next section.

2.3. Distribution of geometrical parameters of random foams

Zhu et al. [24] use a “drop and roll” algorithm [23] to generate random nuclei and studied the geometric properties of the corresponding Voronoi diagram. However the “drop” algorithm can only achieve packing fraction 0.5 for 2D foams. Jullien et al [21] used the rate-dependent algorithm to study the long-range correlation and local order in random packing of spheres via calculation of the two-point correlation function and the Voronoi tessellation. Using a discrete element method, Yang et al. [25] studied the

topological and metric properties of the 3D Voronoi diagram as a function of the packing particle size and fraction.

Here we will discuss the evolution of the geometric properties of the random foams generated from the Voronoi diagram for both 2D and 3D using the rate-dependent algorithm described above. Figure 6 reports the distribution functions of the cell geometrical parameters for a 2D random structure at different packing fractions. The geometrical properties (edge length, vertex angle, cell area and cell perimeter, number of edges) of the cells are normalized by the corresponding parameter of the regular honeycomb cell. The honeycomb cell corresponds to the highest packing fraction ($\phi_c = \frac{\pi}{2\sqrt{3}} \approx 0.9069$) for 2D structures. In Fig. 6(a), the distribution of edge length is shown. For fully random packing of nuclei, the normalized edge length is almost uniformly distributed between 0.0 and 1.5 and no obvious peak can be observed. As the packing fraction increases, a peak above 1 appears and approaches 1. Figure 6(b) shows the distribution of the cell perimeter. In contrast to the edge length shown in Fig. 6(a), the peak position for the cell perimeter is much closer to 1 and has no observable shift as the packing fraction increases. Figure 6(c) presents the distribution for vertex angle which is normalized by the vertex angle 120° for a regular honeycomb. For lower regularity, the distribution peak is above 1 and approaches 1 as regularity increases. Figure 6(d) shows the cell area distribution. As can be seen, the normalized cell area is less than 1 and approaches 1 as regularity increases. Figure 6(e) shows the distribution of edge numbers per cell. One can see that the peak is at 6 which is the edge number for a regular honeycomb. Only the probability at 6 increases as the foam regularity increases. All parameter distributions narrow with increase of the packing fraction and the peak position

is shifted to 1 if the cell parameter is normalized by the packing number of the honeycomb structure. These statistical distributions show that the full random structure evolves to regular honeycomb structures with number of iterations and increase of packing number

Figure 7 shows the density ratio for the random foam generated from the Voronoi diagram. In this calculation, the Voronoi edges are replaced by struts. The width of the strut is selected to make the density ratio for the regular honeycomb structure 0.1. The relative density decreases linearly by 6% as packing fraction increases and can be written by fitting the curve to find the decrease rate

$$\frac{\rho_r}{\rho_h} = 0.08767(\phi_h - \phi_r) + 1, \quad (2)$$

where ρ_r and ρ_h are the relative densities for the random and honeycomb structures respectively. $\phi_h (= 0.9069)$ and ϕ_r are the packing fraction of the random and honeycomb 2D structures respectively. The foam density decreases with packing.

Figure 8 shows the distribution functions for 3D random open foam structures at different packing fractions. For the 3D case, the maximum packing fraction ($\phi_c = \frac{\pi}{3\sqrt{2}} = 0.74$) is given by the face-centered cubic or hexagonal closed packing.

Their corresponding Voronoi diagram is the rhombic dodecahedron cell shown in Fig. 2(b). However, as will be shown below, the final random close packing obtained using the procedure described above does not converge to the face-centered-cubic or the hexagonal-closed-packing structures. Foams with truncated octahedron cells have been widely studied [16, 17], therefore we will normalize the geometrical properties of the cell of the random structures by the parameters of the truncated octahedron, the body centered

packing structure ($\phi_c = \frac{\sqrt{3}\pi}{8} = 0.68$) whose cell is the truncated octahedron (Fig. 2(c)).

In Fig. 8(a), the distribution of edge length is shown. For full random packing of nuclei, the normalized edge length is dominated by short struts. With increase of packing regularity a peak at position larger than 1 starts to appear. As in the 2D case, very short edges still exist in highly regular structures. Figure 8(b) show the distribution of face areas. The area is normalized by the area of the hexagonal face in the truncated octahedron cell. Consistent with the edge length distribution, a significant number of faces have small area and the peak appears at slightly below 1. Figure 8(c) shows the distribution of vertex angle which is normalized by 120° , the vertex angle for the truncated octahedron cell. This distribution is very similar to the 2D case shown in Fig. 6(b). The distributions of the surface area and volume of the Voronoi cells are shown in Figs. 8(c, d). Compared to Figs 8(a, b, c), these properties have much narrow distributions and sharper peaks. Figures 8 (f, g) show the distribution of number of facets per cell and number of edges per facet. The truncated octahedron has 14 facets per cell, 6 of which are square and 8 hexagonal. The numbers corresponding to the truncated octahedron are indicated in Fig. 8(f, g) by the dotted lines. The peak for number of facets per cell is 15. The average number of facets per cell decreases from 15.35 to 14.25 when the packing fraction increases from 0 to 0.64. Figure 9 shows the density ratio versus packing fraction. In this calculation the Voronoi edges are replaced by thin struts. The width of the strut is selected to make the density ratio for the truncated octahedron foam 10%. The density decreases by 10% as packing fraction increases. As in the 2D case, one may approximate the relation between the density ratio and packing fraction with a linear function:

$$\frac{\rho_r}{\rho_t} = 0.08767(\phi_t - \phi_r) + 1, \quad (3)$$

where ρ_r and ρ_t are the relative densities for the random and truncated octahedron structures respectively. $\phi_h (= 0.68)$ and ϕ_r are the packing fractions of the random and truncated octahedron 3D structures respectively.

3. Analytical and Numerical Methods to Determine Elastic Properties of Foams

Different approaches have been used for the homogenization of heterogeneous media and obtaining their effective elastic properties [10]. Here we will apply the principle of minimum potential energy [9, 10] to estimate the effective properties of foams. In this approach, we first simulate a foam structure bounded by a square for 2D and a cubic for 3D with periodic boundary conditions. Then all struts in the foam are modeled by plane or spatial beams using 2-nodes elements considering axial, bending and torsion deformations [26]. The strain energy of the system is calculated as the summation of the energy for each individual beam using the finite element method for spatial beams and the total strain energy U_B is written as

$$U_B = \frac{1}{2} \mathbf{D}^T \mathbf{K} \mathbf{D}, \quad (4)$$

where \mathbf{D} is the general displacement vector of the nodes which include axial, bending and torsion displacements; \mathbf{K} is the global stiffness matrix.

We consider that the macroscopic strain γ_{ij}^0 and stress σ_{ij}^0 are known at the computation domain boundary determining the boundary conditions. If assuming

macroscopic strain γ_{ij}^0 ($\gamma_{ij}^0 = \varepsilon_{ij}^0$ for $i = j$ and $\gamma_{ij}^0 = 2\varepsilon_{ij}^0$ for $i \neq j$), the periodic boundary conditions are written as the relation between the displacements ($u_{i0}, u_{i1}, i=1, 2, 3$) at the opposite side of the computation domain (square for 2D and cube for 3D)

$$u_{i0} - u_{i1} = \varepsilon_{ij}^0 (x_{j0} - x_{j1}), \quad (5)$$

where x_{i0} and x_{i1} are the coordinates of the boundary nodes at the opposite side. For given macroscopic strain, one may also use constrained boundary conditions. In this case, the displacement at the boundary is given as

$$u_i = \varepsilon_{ij}^0 x_j, \quad (6)$$

where x_j is the coordinate of the boundary nodes. The bending moments at these nodes are assumed to be zero. For given macroscopic stresses σ_{ij}^0 , we calculate the force for the beam nodes lying on the boundary surfaces. For example, considering area A_c with N nodes on the boundary surface, the force in each node is $\sigma_{ij}^0 A_c / N$ and the moment is zero (due to constant stresses σ_{ij}^0). Using different boundary conditions may have different results [27].

After applying the boundary conditions the total strain energy (Eq. 4) of the system is obtained and is minimized using the fast conjugate gradient method. Alternatively one can also formulate the global finite element stiffness matrix for the system and solve the linear system of equations to obtain the equilibrium state whose corresponding strain energy represents the minimum values.

After the minimum strain energy is obtained, the effective elastic stiffnesses or compliances are calculated by comparing them with those of an effective homogeneous medium. The strain energy of a homogeneous medium for given strains ϵ_{ij}^0 is given by

$$U_\epsilon = \frac{1}{2} \epsilon_{ij}^0 C_{ijkl} \epsilon_{kl}^0 V_\epsilon, \quad (7)$$

where C_{ijkl} is the effective stiffness tensor; V_ϵ is the volume of the structure. For given constant stress σ_{ij}^0 , the strain energy of the effective homogeneous medium is given by

$$U_\sigma = \frac{1}{2} \sigma_{ij}^0 S_{ijkl} \sigma_{kl}^0 V_\epsilon, \quad (8)$$

where S_{ijkl} is the effective compliance tensor. Equating the strain energy obtained by the beam model ($U_B = U_\epsilon = U_\sigma$), we obtain the effective stiffness tensor for constant strain and the effective compliance tensor for constant stress. For example, for a 2-D problem the strain energy for the effective medium may be written as

$$U_\epsilon = V_\epsilon ((\epsilon_{11}^0)^2 C_{1111} + (\epsilon_{22}^0)^2 C_{2222} + 2\epsilon_{11}^0 \epsilon_{22}^0 C_{1122} + (\gamma_{12}^0)^2 C_{1212}) / 2. \quad (9)$$

If ϵ_{11}^0 is given and other strain components are zero, one obtains $C_{1111} = 2U_\epsilon / (V_\epsilon \epsilon_{11}^0{}^2)$.

Similarly one can obtain other constants.

If the bounded structure includes a large number of struts, then the solution can only be obtained numerically. However for regular foams shown in Figs. 1 and 2, we have obtained simple analytical solution for the smallest cell in the foam using symbolic software. The results are discussed in the next two sections.

For foams with multiple cell structures, one can first formulate the stiffness/compliance matrix for each cell and then obtain the elastic constants for the foams based on the connection of the cells.

4. Foams with 2-D Microstructures

The elastic properties for 2D regular foam have been widely investigated [2, 15, 14]. Here we use the method described in section 3 to derive the analytical elastic constants for 2-D foams. Differently from other approaches, we write the elastic constants in compliance form with shear deform correction. Therefore they could be used for forms with relatively larger thickness to length ratio or larger density ratio. We apply the algorithm described in section 3 for 2-D orthogonal, triangle and general honeycomb unit cells shown in Fig. 1. The analytic compliances for the unit cell shown in Fig. 1 are listed in Tables 1-3. All the compliances can usually be separated into two terms corresponding to bending and extension respectively. The entire cell compliance matrix S_{ij}^C can be written in the form as

$$\frac{S_{ij}^C}{S_s} = \frac{C}{A} + \frac{B}{I}, \quad (10)$$

where A is the cross-section area, I is the second moment of the cross section area and $S_s = 1/E_s$ (E_s is the modulus of the frame). Here we assume the second moments of area about the x and y axis are the same. The two parameters C and B depend on the geometry of the cell. The first term corresponds to axial compliance and the second to bending compliance. Tables 1-3 list the expressions for C and B for 2-D for orthogonal, triangle and general honeycomb cells. In these tables Φ_y is the shear correction constant in the y axis [26]. The results obtained from the macroscopic strain or stress approaches are identical. Usually the solution based on the macroscopic strain approach is more simply implemented than the macroscopic stress approach. This is because in the macroscopic

strain approach, the displacement at the boundary can be simply obtained using Eqs. (5 or 6). In the macroscopic stress approach, one needs to determine the forces at each boundary node and pay special attention to the corner boundary nodes which lie on multiple boundary surfaces; proper constraint must also be introduced to assure uniqueness of the solution.

Table 1 lists the expression for C and B for the orthogonal cell (Fig. 1a). For this cell, there is no bending effect on the compliance components for S_{11} and S_{22} . For S_{44} , the cell compliance is determined only by the bending. Obviously, for this structure the Poisson's ratio is zero which leads to zero S_{12} . Table 2 shows the parameters for a triangular cell (Fig. 1b). For this structure, all compliances can be written in the form of an extension effect but C is dependent on the bending moment I . Table 3 gives the parameters for a general honeycomb cell. It shows that the extension and bending coefficients C and B depend on the angles between the struts θ .

The foam structures shown in Fig. 1 are formed by only one unit cell, given at the bottom of these figures. The compliances listed in Table 1-3 also represent the compliances for the corresponding foam structures. To show the accuracy of the analytical equations, we calculated the elastic properties for the foam structures with $27*27$ cells by solving the system numerically. Figure 11 compares the Young's modulus E_{11} and shear modulus G_{12} for a cellular structure with square cells ($L=L_x=L_y$) at different strut widths t . It shows that the analytical and numerical results are identical. As expected, the Young's modulus is a linear function of t/L and the shear modulus is proportional to $(t/L)^3$. Figure 12 compares the Young's modulus E_{11} and shear modulus G_{12} for a cellular structure with triangular cells. The two solutions give almost identical

results. Both moduli have nearly linear relation with t/L . Figure 13 presents the results for a structure with regular hexagonal cells ($\theta=30^\circ$). The analytical and numerical solutions are slightly different from each other and the discrepancy increases as t/L increases. It has been observed that the numerical solution will converge to the analytical solution with increase of number of cell in the cellular structures. Therefore we believe this discrepancy is introduced by the disturbing of the struts on the boundaries. Further comparison for general hexagonal cells is given in Fig. 14 for cells with different θ . For $t/L=0.2$ the solutions are compared with the analytical equations given in [2, 14]. This shows that the analytical compliances given in Table 3 have very good agreement with the numerical results calculated using $27*27*27$ cells for all angles θ . When the angles become negative, the Poisson's ratio becomes negative also (the so-called reentrant structures [19]).

It is useful to represent the elastic properties in terms of the density ratio. For low density foams ($t/L \ll 1$) and neglecting the shear correction constant, one can obtain the S_{11} and S_{44} for square foams as

$$S_{11} = \frac{2}{\rho}, S_{44} = \frac{4}{\rho}. \quad (11)$$

S_{11} , S_{12} and S_{44} for triangular foams as

$$S_{11} = \frac{3}{\rho}, S_{12} = -\frac{1}{\rho}, S_{44} = \frac{8}{\rho}. \quad (12)$$

S_{11} , S_{12} and S_{44} for regular honeycomb foams as

$$S_{11} = \frac{3}{2\rho} + \frac{2}{3\rho^3}, S_{12} = \frac{1}{2\rho} - \frac{2}{3\rho^3}, S_{44} = \frac{2}{\rho} + \frac{8}{3\rho^3}. \quad (13)$$

Equations (11, 12 and 13) are identical with those shown in refs. 2 and 4. However, the compliance list in tables 1-3 can apply to foams with relative higher density ratio.

5. Foams with 3-D Microstructures

As for two-dimensional structures, we apply the algorithm described in section 3 for 3-D orthogonal, rhombic dodecahedron and truncated octohedron structures shown in Fig. 2. The unit cell for these three structures are shown at the bottoms of Fig. 2. The compliances obtained for these unit cells are listed in Table 4-6. Similarly to the two-dimensional compliance matrices, the three-dimensional compliances also can be decomposed to axial (C) and bending (B) compliances and the results obtained from the macroscopic strain and stress approaches are identical. The Voronoi unit cells for rhombic dodecahedron and truncated octahedron are not the smallest repeating cells of the corresponding structures. From the structure of each node, one can find the smallest repeating cells which are shown in Figure 16 (a) for rhombic dodecahedron and (b) truncated octahedron. The effective elastic properties of the foams with truncated octahedron cell structures have been studied based on stress analysis using the structural beam model [16, 17].

Table 4 gives the formulations of C and B for a 3-D orthogonal cell shown of the bottom of Fig. 2(a). For this cell there is no bending compliance for S_{ii} ($i=1,2,3$), while for the shear compliances (S_{44} , S_{55} and S_{66}) are determined only by bending. Obviously, for this structure the Poisson's ratio is zero which leads to zero S_{12} . For the rectangular-parallelepiped cellular structures shown at the top of Fig. 2(a), there is only the orthogonal cell, therefore the cell compliances shown in Table 4 also represent the

compliance for the cellular structures. We compared it with numerical results calculated using $8*8*8$ cells. The comparison is shown in Fig. 15.

Table 5 shows the compliances for the smallest periodic cell (Fig. 3(b)) of the cellular structures with rhombic dodecahedron cells. The rhombic dodecahedron cellular structure is formed by the cell given in Fig. 3(b) with a same-size vacuum. Therefore the compliances for this cellular structure will be twice the compliances given in Table 5. The comparison with numerical results calculated using $8*8*8$ cells are shown in Fig. 17.

Table 6 shows the compliances for the smallest periodic cell (Fig. 2(c)) of the cellular structures with truncated octahedron cells. As shown in Figure 2(c), each node has the same structure as the smallest cell shown in Fig. 16(b). However half of the nodes whose corresponding structures is rotated by 90 degree from the cell given in Fig. 16(b). Therefore the compliances S_{ij}^F and Poisson's ratio ν_{13}^F for this cellular material are given by

$$S_{33}^F = (S_C(1,1) + S_C(3,3))/2, \quad S_{44}^F = (S_C(4,4) + S_C(5,5))/2,$$

$$\nu_{13}^F = -\frac{S_C(1,3)}{S_C(3,3)}, \quad (14)$$

Comparison with numerical results is given in Fig. 18.

As in the 2D case, one may represent the elastic properties in terms of density ratio for low-density foams ($t/L \ll 1$) by neglecting the shear correction constant.

6. Effect of randomness

All practical foams have a certain degree of randomness. The effects of non-periodic microstructure on the elastic properties of 2D and 3D foams are studied by using

a “drop” nuclei algorithm and Voronoi tessellation to generate foams with different regularities [8, 14, 28]. The effect of microstructural heterogeneities on the elastic modulus and yield strength has also been investigated by introducing random perturbations into the regular honeycomb foams [29]. All these simulations show that randomness introduces modulus increases. The aim of this section is to investigate quantitatively the relation between elastic properties and packing fraction using the algorithm described in section 2, where we showed that the packing fraction is a good parameter to describe the regularity of a random structure. At low regularity, the geometric properties (size, shape) vastly differ among the cells in the foam. As the packing fraction increases, the cells become more uniform and resemble the hexagon in 2D and the truncated octahedron in 3D. Therefore packing fraction may be used as a scaling factor to relate the elastic properties between random and regular foams.

6.1 Elasticity of 2D random foams

Using the microstructure simulation algorithm described in section 2, we obtain 18 sets of independent microstructures for each packing density. Replacing each edge by a uniform strut we obtain foam structures with different regularities. Here we use constant density ratio for all random structures to avoid the density ratio decrease with packing fraction when the cross section area of the strut is a constant. Therefore we vary the cross section area to keep the density ratio constant; i. e. the cross section area increases when the packing fraction increases. Each edge is modeled by one beam element and using the algorithm described in section 3, we obtain the elastic properties of the foams.

Figures 19(a, b, c) show the Young's modulus, shear modulus and Poisson ratio variation as packing density increases. The density ratio of the foam is 0.1. Each solid line represents one independent data set. The average value is shown by the thick solid line with open circles. The Young's modulus and shear modulus decrease as packing density increases. The change from the fully random state to the random closed packing state is about 30% for both Young's modulus and shear modulus. The Poisson ratio slightly increases as packing fraction increases (only about 3% change). The scattering of the data is greater at lower packing fractions.

In Figure 20 we show the modulus as a function of density ratio for different packing fraction. Comparing this figure with Fig. 13 for honeycomb structure, one sees that the relation between modulus and density ratio is similar. In section 3, we show that the compliances of a given structure can be expressed as a summation of bend and axis compliances. For random structures, we may also decompose the compliance into bending and axis deformation effects

$$\begin{aligned}
 1/E &= \frac{D_R^E}{\rho} + \frac{B_R^E}{\rho^3} \\
 1/G &= \frac{D_R^G}{\rho} + \frac{B_R^G}{\rho^3}
 \end{aligned}
 \tag{15}$$

The parameters D_R^E , B_R^E , D_R^G and B_R^G can be found by fitting the curves given in Figure 20. These parameters are functions of foam geometrical properties which can be categorized by the packing fraction. Figure 20(a) shows the fitting of the data obtained by the FEM method (open symbols) using Eq. (15) (solid lines). The parameters obtained are shown in Figure 21. The bending parameters B_R^E and B_R^G increase as packing fraction

increases while the axis deformation parameters D_R^E and D_R^G decrease. Their average value may be approximated as linear functions of the packing fraction:

$$\frac{D_R^E}{D_h^E} = 1.18(\phi_h - \phi_r) + 1, \quad \frac{B_R^E}{B_h^E} = -0.341(\phi_h - \phi_r) + 1 \quad (16)$$

$$\frac{D_R^G}{D_h^G} = 3.088(\phi_h - \phi_r) + 1, \quad \frac{B_R^G}{B_h^G} = -0.277(\phi_h - \phi_r) + 1 \quad (17)$$

where $D_h^E (=3/2)$, $B_h^E (=2/3)$, $D_h^G (=2)$ and $B_h^G (=8/3)$ are the corresponding parameters for the regular honeycomb structure. Therefore, using the packing fraction, we statistically correlated the elastic properties for the regular honeycomb to fully random structures.

6.2 Elasticity of 3D random foams

As in the 2D case, we simulated 18 sets of independent microstructure for each packing density using the algorithm described in Section 2. Each edge is modeled by a beam element and using the algorithm described in section 3, we obtain the elastic properties of the foams.

Figures 22(a, b, c) show the Young's modulus, shear modulus and Poisson ratio change as packing density increases. The density ratio of the foam is 0.1. As in the 2D case the Young's modulus and shear modulus decrease as packing density increases and the Poisson ratio slightly increases. Because the cell number is smaller, the scattering is much greater in the 3D case.

7. Conclusion

In this report analytical and numerical methods to estimate the effective elastic properties of regular and random open-cell foams have been developed. The methods are based on the principle of minimum energy and on structural beam models. The analytical solutions are obtained by symbolic solution of the system. The microstructure of the foams is simulated using Voronoi tessellation. By comparing with solid finite element solution, the applicability of the solution based on the beam model has been discussed. The effect of randomness is also discussed.

Acknowledgements

This work was sponsored by the NASA under contract#DTFA03-98-D-00008. Dr. William T. Yost is the project manager.

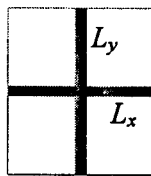
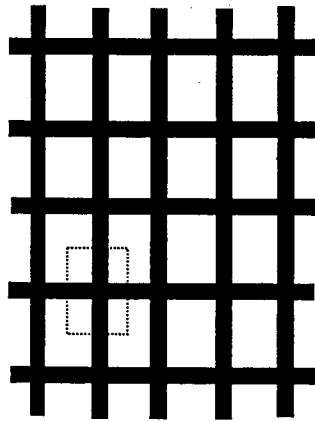
References

- [1] J. Banhart, "Manufacture, characterization and application of cellular metals and metal foams," *Progress in Materials Science*, 46, 559-632 (2001).
- [2] L. J. Gibson and M. F. Ashby, *Cellular solids: Structure and Properties*, Cambridge U. Press, Cambridge, UK (1997).
- [3] I. F. Sadoc and N. Rivier (ed.), *Foams and Emulsions*, Kluwer Academic, Boston, 1999.
- [4] R. M. Christensen, "Mechanics of cellular and other low density materials," *Int. Solids and Struct.*, 37, 93-104 (2000).
- [5] L. Helfen, T. Baumbach, H. Stanzick, J. Banhart, A. Elmoutaouakkil, and P. Cloetens, "Viewing the early stages of metal foam formation by computed

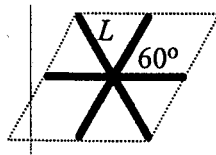
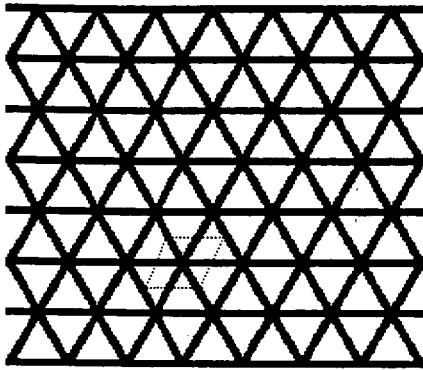
- tomography using synchrotron radiation,” *Advanced Engineering Materials* 4, 808-813d (2002).
- [6] B. N. Boots, “The arrangement of cells in random networks,” *Metallography*, 15, 53-62 (1982)
- [7] M. W. D. Van der Burg, V. Shulmeister, E. Van der Geissen, R. Marissen, “On the linear elastic properties of regular and random open-cell foam models,” *J. Cell. Plast.* 33, 31-53 (1997).
- [8] H. X. Zhu, J. R. Hobdell, and A. H. Windle, “Effects of cell irregularity on the elastic properties of open-cell foams,” *Acta. Mater.* 48, 4893-4900, 2000.
- [9] A. P. Roberts and E. J. Garboczi, “Elastic properties of model random three-dimensional open cell solids,” *J. of Mech. Phys. Solids* 50, 33-55 (2002).
- [10] S. Torquato, *Random Heterogeneous Materials: Microstructure and Macroscopic Properties*, Springer, New York, 2002.
- [11] A. P. Roberts, “Statistical reconstruction of three-dimensional porous media from two-dimensional images,” *Physical Review E*, 56, 3023-3034 (1997).
- [12] W. E. Warren and A. M. Kraynik, “The linear elastic properties of open-cell foams,” *J. Appl. Mech.* 55, 341-346, (1988).
- [13] W. E. Warren and A. M. Kraynik, “Foam mechanics: the linear elastic response of two-dimensional spatially periodic cellular materials,” *Mech. Mater.* 6, 27-37 (1987)
- [14] M. J. Silva, W. C. Hayes and L. J. Gibson, “The effect of non-periodic microstructure on the elastic properties of two-dimensional cellular solids,” *Int. J. Mech. Sci.* 37, 1161-1177 (1995).

- [15] R. M. Christensen, "The Hierarchy of Microstructures for Low Density Materials",
Z. Angew. Math. Phys., Vol. 46, pp 5506-5521 (1995).
- [16] H. X. Zhu, J. F. Knott, and N. J. Mills "Analysis of the elastic properties of open-cell foams with tetrakaidecahedral cells," J. Mech. Phys. Solids 45, 319-343 (1997).
- [17] W. E. Warren and A. M. Kraynik, "Linear elastic behavior of a low-density Kelvin foam with open cells," J. Appl. Mech. 64,787-794 (1997).
- [18] C. B. Barber, D. P. Dobkin, and H. T. Huhdanpaa, The Quickhull algorithm for convex hulls, ACM Trans. on Mathematical Software, Dec. 1996.
- [19] D. Stoyan, W. S. Kendall, and J. Mecke. Stochastic geometry and its applications. Chichester: John Wiley & Sons, 1995.
- [20] W. S. Jodrey and E. M. Tory, "Computer simulation of close random packing of equal spheres," Phys. Rev. A 32, 2347-2351 (1985).
- [21] R. Jullien, P. Jund and D. Caprion, "Computer investigation of long-range correlations and local order in random packings of spheres," Phys. Rev. E. 54, 6035-6041 (1996).
- [22] J. Tobochnik and P. M. Chapin, J. Chem. Phys. 88, 5824 (1988).
- [23] W. M. Visscher and M. Bolsterli, Nature, 239, 504 (1972).
- [24] H. X. Zhu, S. M. Thorpe and A. H. Windle, "The geometrical properties of irregular two dimensional Voronoi tessellations," Philosophical magazine A, 81, 2765-2783, 2001.
- [25] R. Y. Yang, R. P. Zou and A. B. Yu, "Voronoi tessellation of the packing of fine uniform spheres," Phys. Rev. E 65, 041302-041310(2002).

- [26] J. S. Przemieniecki, Theory of matrix structural analysis, New York, McGraw-Hill 1968.
- [27] C. Chen, T. J. Lu and N. A. Fleck, "Effect of imperfection on the yielding of two dimensional foams," *J. Mech. Phys. Solids* 47, 2235-2272 (1999).
- [28] H. X. Zhu, J. R. Hobdell and A. H. Windle, "Effects of cell irregularity on the elastic properties of 2D Voronoi honeycombs," *J. Mech. Phys. Solids* 49, 857-870 (2001).
- [29] A. Fazekas, R. Dendievel, L. Salvo and Y. Brechet, "Effect of microstructural topology upon the stiffness and strength of 2D cellular structures," *Inter. J. Mech. Sci.* 44, 2047-2006 (2002).
- [30] S. Torquato, L. V. Gibiansky, M. J. Silva and L. J. Gibson, "Effective mechanical and transport properties of cellular solids," *Int. J. Mech. Sci.* 40, 71-82 (1998).
- [31] R. S. Lakes, "Materials with structural hierarchy", *Nature*, 361, 511-515 (1993).
- [32] C. Chen, T. J. Lu and N. A. Fleck, "Effect of inclusions and holes on the stiffness and strength of honeycombs," *Int. J. Mech. Sci.* 43, 487-504 (2001).
- [33] A. E. Simone and Gibson L. J., "The effects of cell face curvature and corrugations on the stiffness and strength of metallic foams," *Acta Materialia*, 46, 3929-3935 (1998).



(a)



(b)

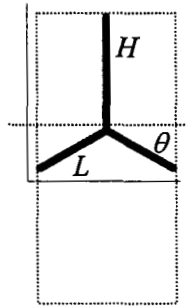
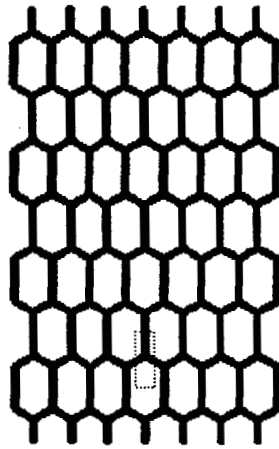
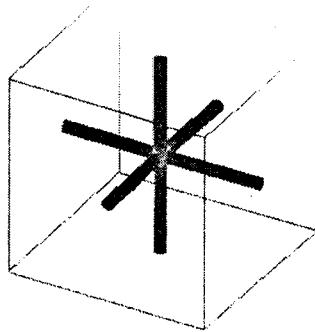
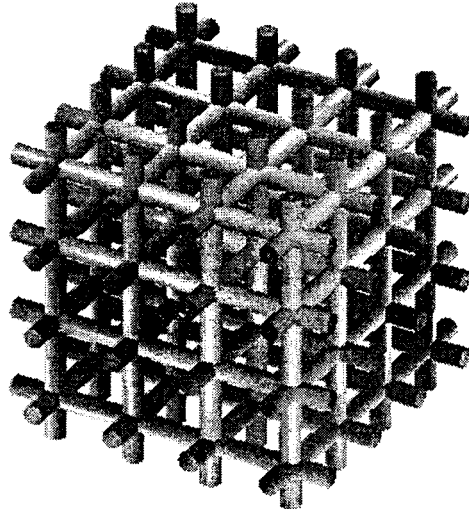
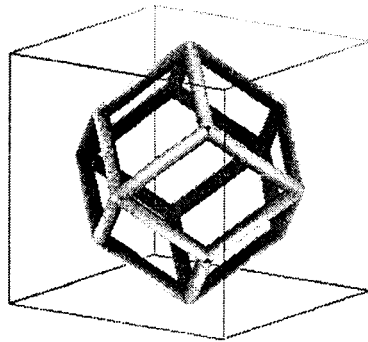
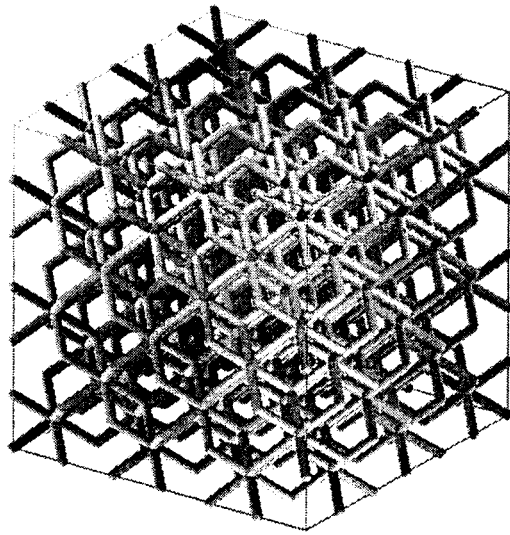


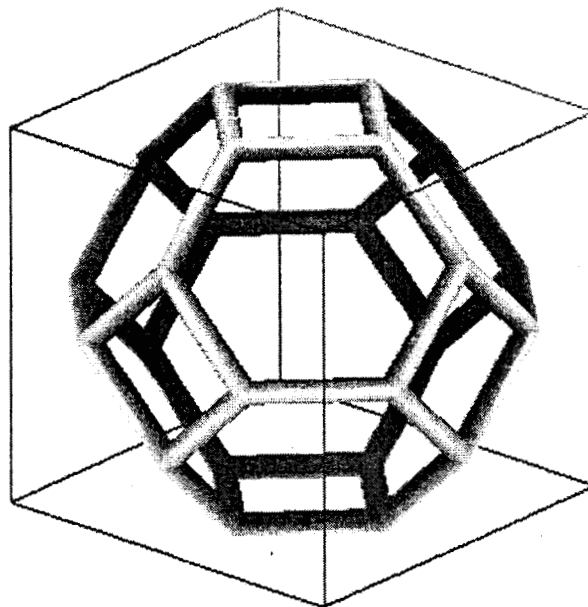
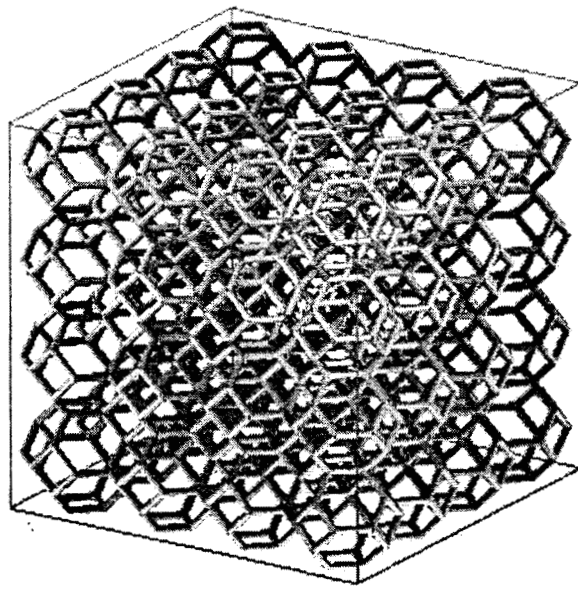
Figure 1. 2-D microstructures. (b) Rectangle. (b) Triangle. (c) General honeycomb.



(a)



(b)



(c)

Figure 2. 3-D microstructures. (a) Cubic. (b) Rhombic dodecahedron. (c) Truncated octahedron.

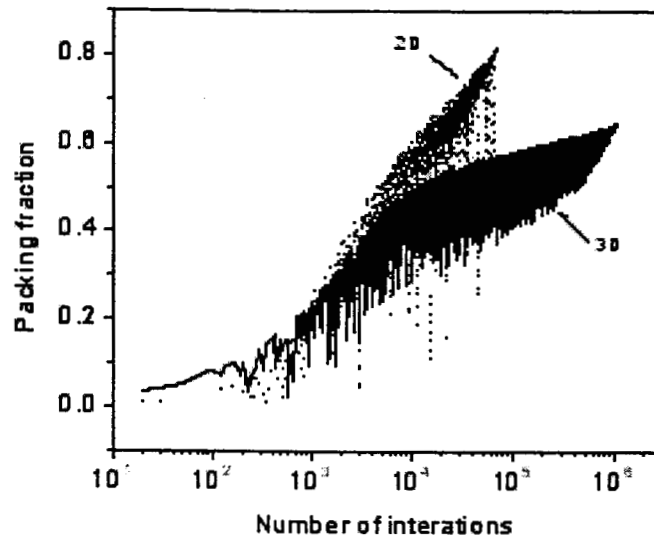
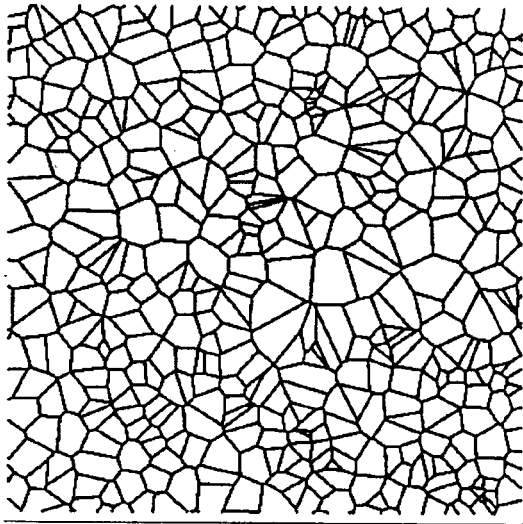
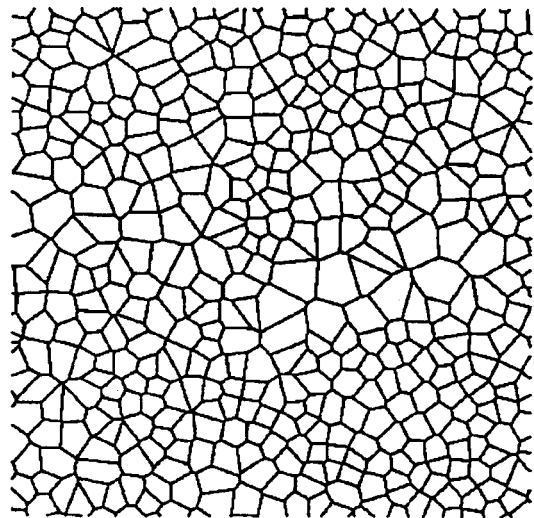


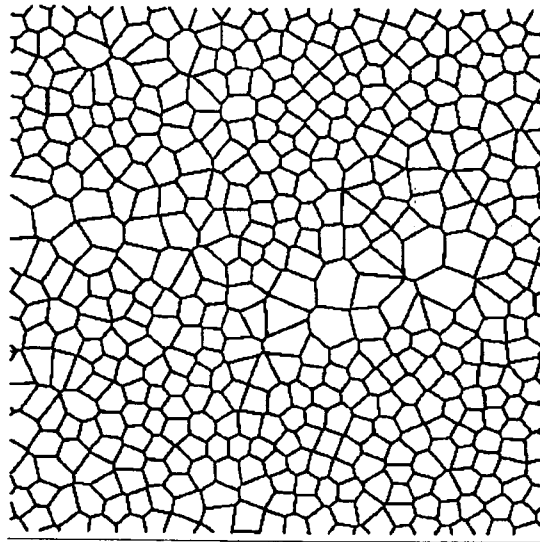
Fig. 3. Evolution of the packing fraction f_i for 2D (dotted line) and 3D (solid line).



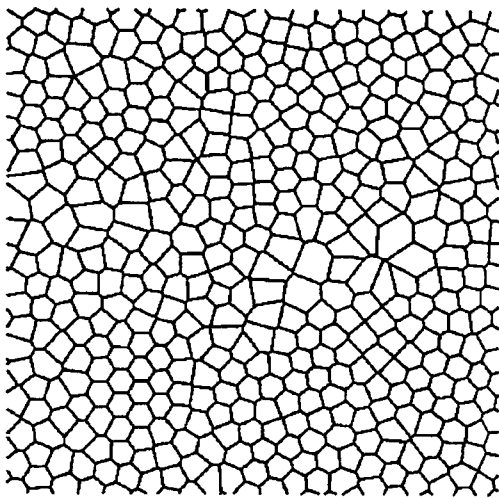
$F_c = 0.0$



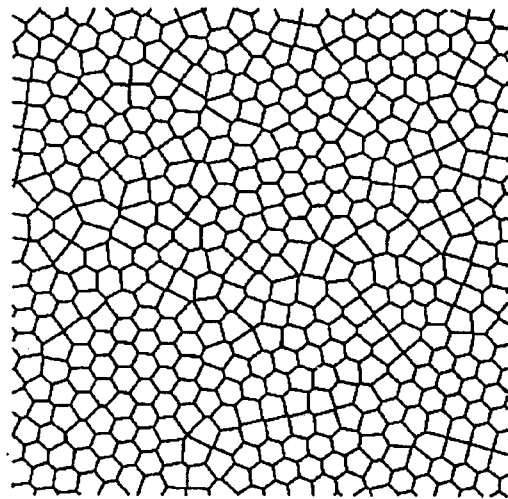
0.2



0.4

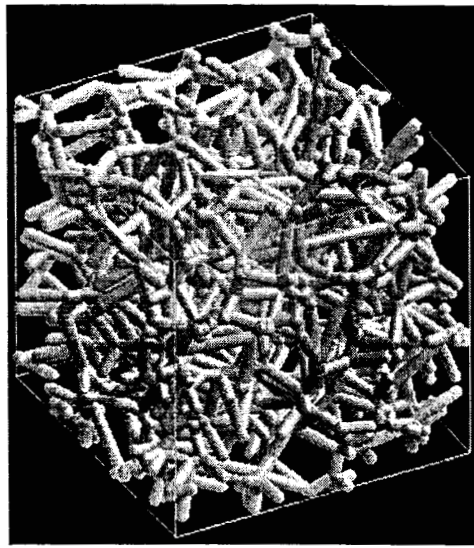


0.6

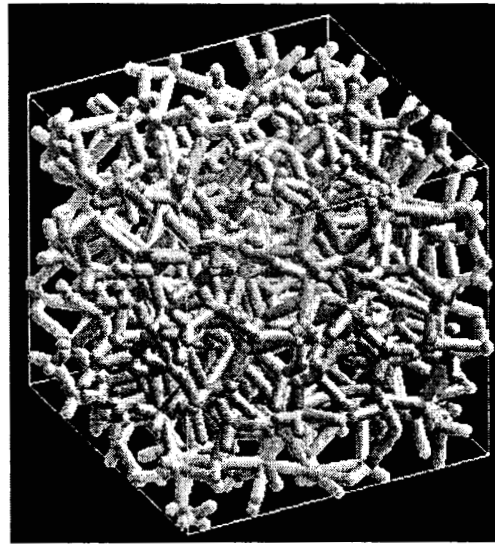


0.816

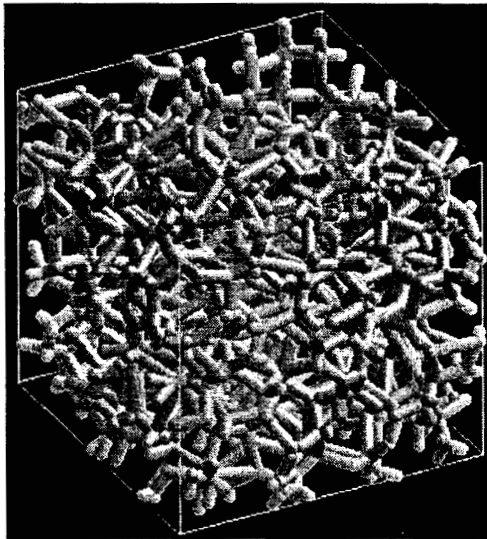
Figure 4. Evolution of 2-D foam microstructure as packing fraction F_c increases. Simulated using 1000 random points in a unit square area.



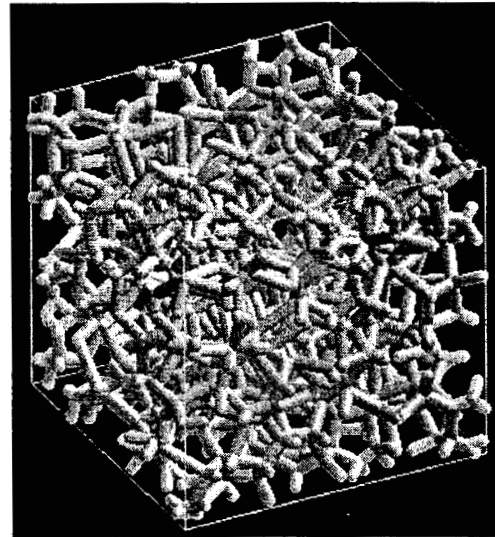
0.0



0.2

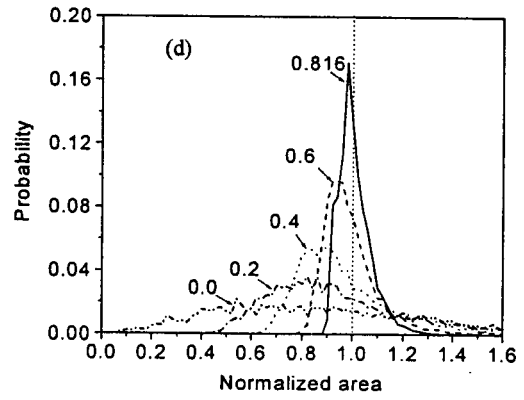
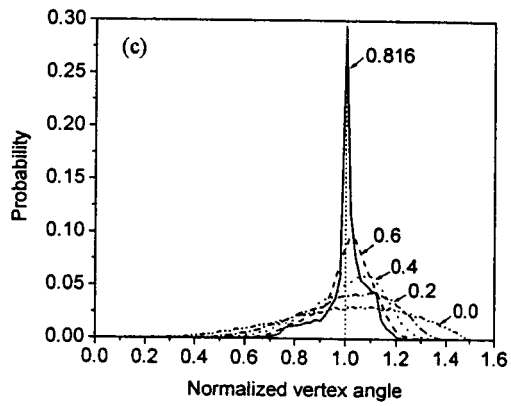
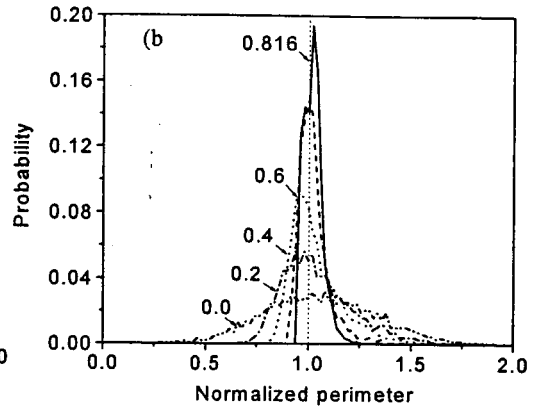
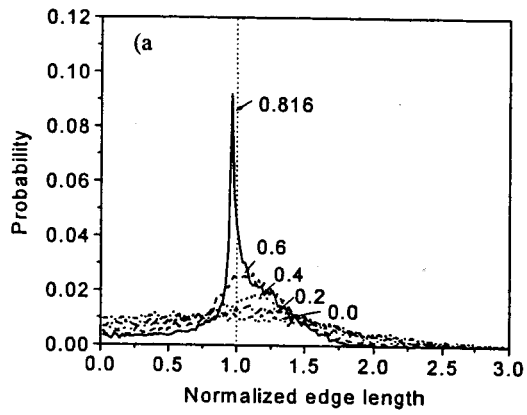


0.4



0.64

Figure 5. Evolution of 3-D foam microstructure as packing fraction F_c increases. Simulated using 1000 random points in a unit square area.



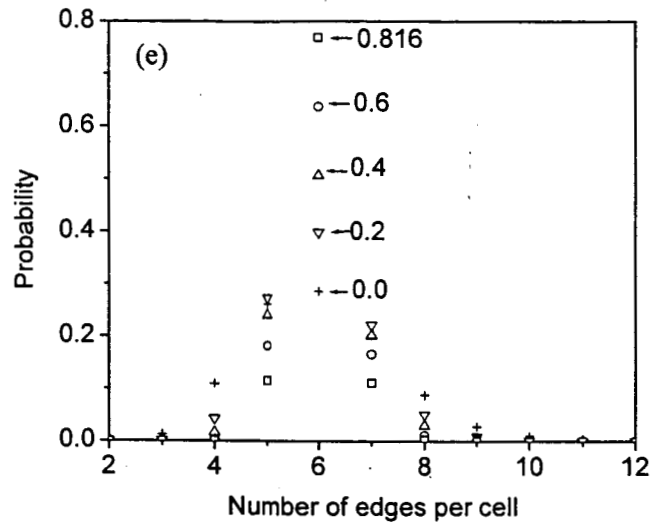


Figure 6. Statistics of 2D random Voronoi diagram for different regularities. (a) strut length distribution, (b) cell perimeter length, (c) cell area distribution. (d) strut angle distribution, (e) number of edges per cell.

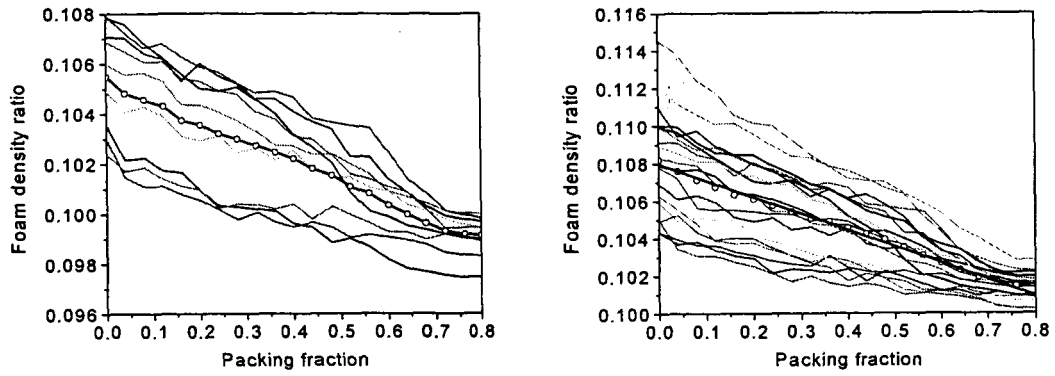
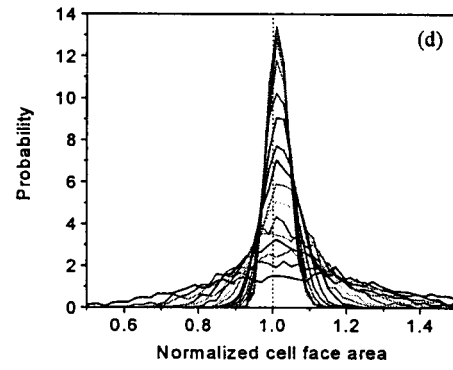
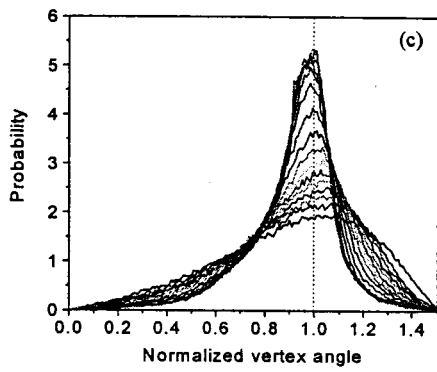
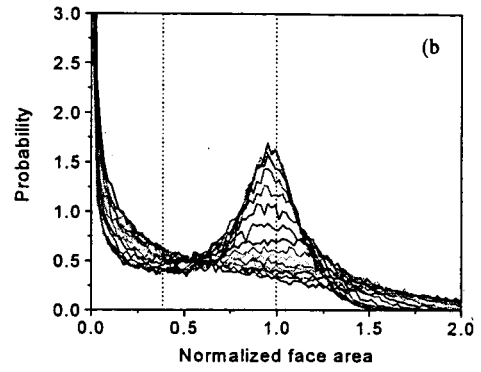
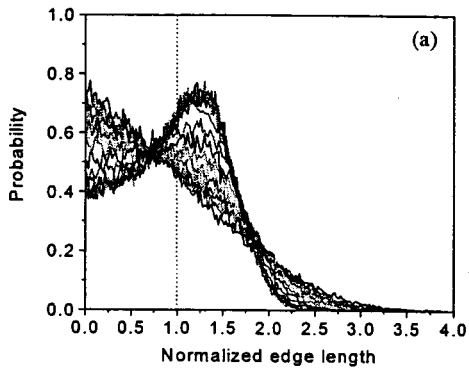
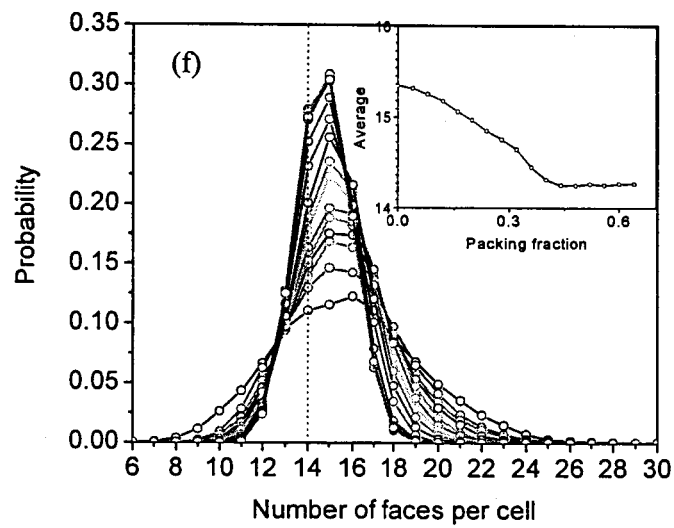
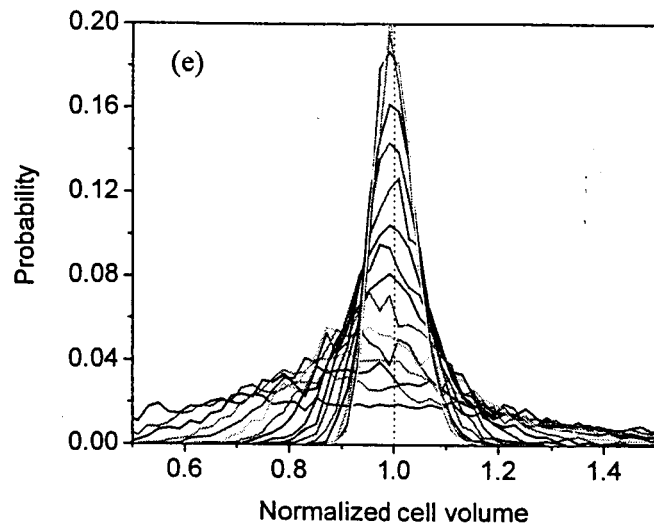


Figure 7. 2-D foam density ratio versus random packing fraction for constant strut cross section. Thin solid lines correspond to independent random structures at different packing fraction. The open circles represent the average, the thick solid lines the linear approximation.





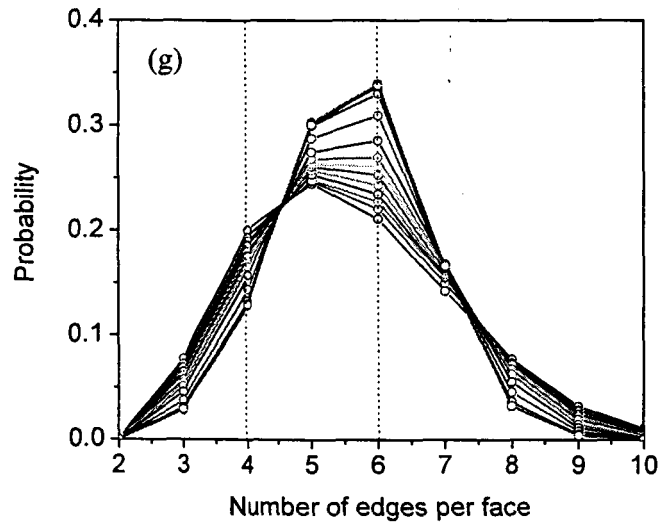


Figure 8. Statistics of 3D random Voronoi diagram for different regularities. (a) edge length distribution, (b) face area distribution, (c) vertex angle distribution, (d) cell face area distribution, (e) cell volume length, (f) number of faces per cell, (g) number of edges per face.

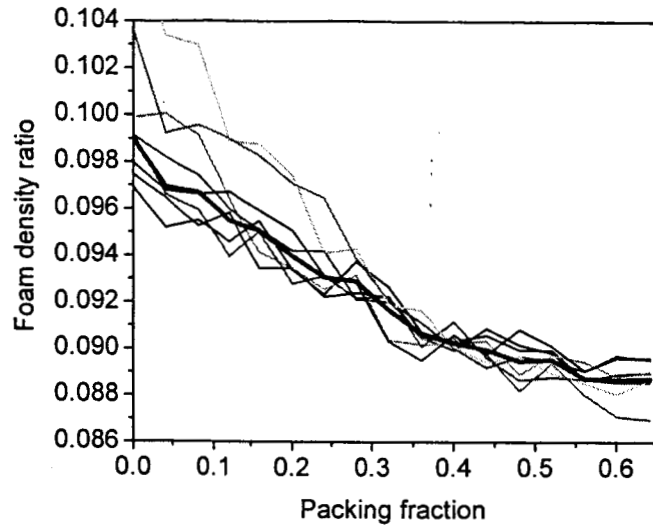


Figure 9. 3-D foam density ratio versus random packing fraction. Nine sets of random structures are calculated at each packing fraction. The thick line represents the average. The cross section of the strut is 0.0024

Compliances	C	B
S_{11}	$2 L_y$	0
S_{22}	$2L_z$	0
S_{12}	0	0
S_{44}	0	$\frac{L_z L_y (L_z + L_y)(4 + \Phi_y)}{6}$

Table 1. Cell compliances for general rectangular 2-D structures.

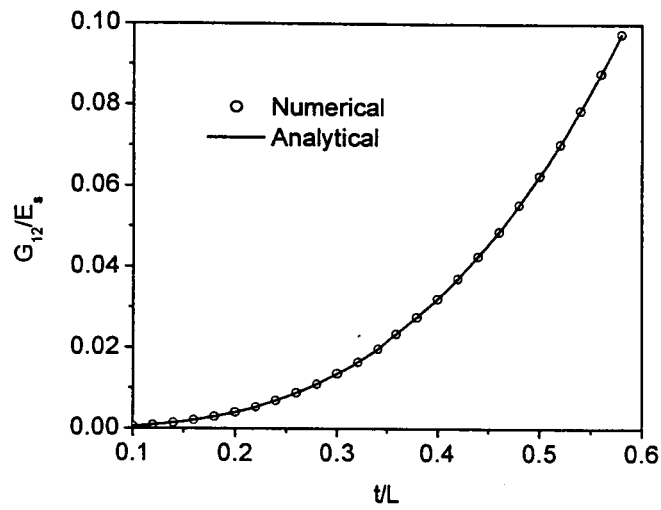
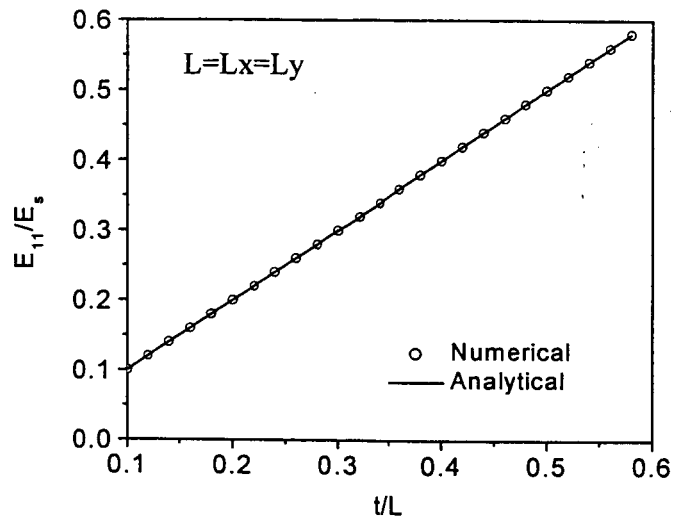


Figure 11. Comparison of elastic properties calculated numerically using $8*8*8$ cells and the analytical results listed in Table 1.

Compliances	C	B
$S_{11} = S_{22}$	$\frac{4I + AL^2(\Phi_y + 4)}{12I + AL^2(\Phi_y + 4)} \sqrt{3}L$	0
S_{12}	$\frac{12I - AL^2(\Phi_y + 4)}{12I + AL^2(\Phi_y + 4)} \frac{L}{\sqrt{3}}$	0
S_{44}	$\frac{AL^2(\Phi_y + 4)}{(12I + AL^2(\Phi_y + 4)) \sqrt{3}} \frac{8L}{\sqrt{3}}$	0

Table 2. Cell compliances for general triangular 2-D structures.

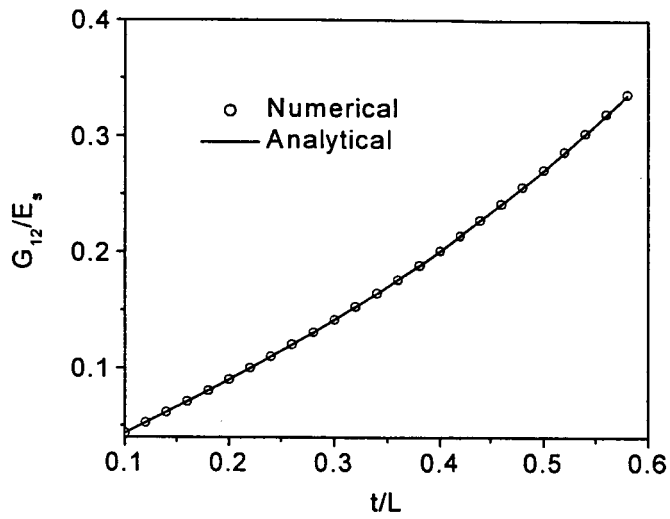
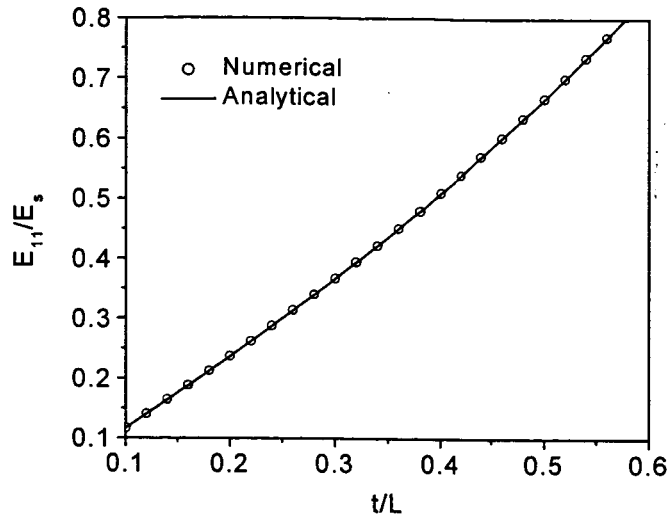


Figure 12. Comparison of elastic properties calculated numerically using 8*8*8 cells and the analytical results listed in Table 2.

Compliances	C	B
S_{11}	$2 \cos(\theta) (L \sin(\theta) + H)$	$\frac{(4 + \Phi_y) \sin^2(\theta) L^2 (L \sin(\theta) + H)}{6 \cos(\theta)}$
S_{22}	$\frac{2L \cos(\theta) (L \sin^2(\theta) + 2H)}{(L \sin(\theta) + H)}$	$\frac{(4 + \Phi_y) L^4 \cos^3(\theta)}{6(L \sin(\theta) + H)}$
S_{12}	$2L \cos \theta \sin \theta$	$\frac{(4 + \Phi_y) L^3 \cos \theta \sin \theta}{6}$
S_{44}	$\frac{2(L + H \sin(\theta))^2}{\cos(\theta)(H + L \sin(\theta))}$	$\frac{(4 + \Phi_y) L H^2 \cos(\theta)(2H + L)}{6(H + L \sin \theta)}$

Table 3. Cell compliances for general hexagon 2-D structures.

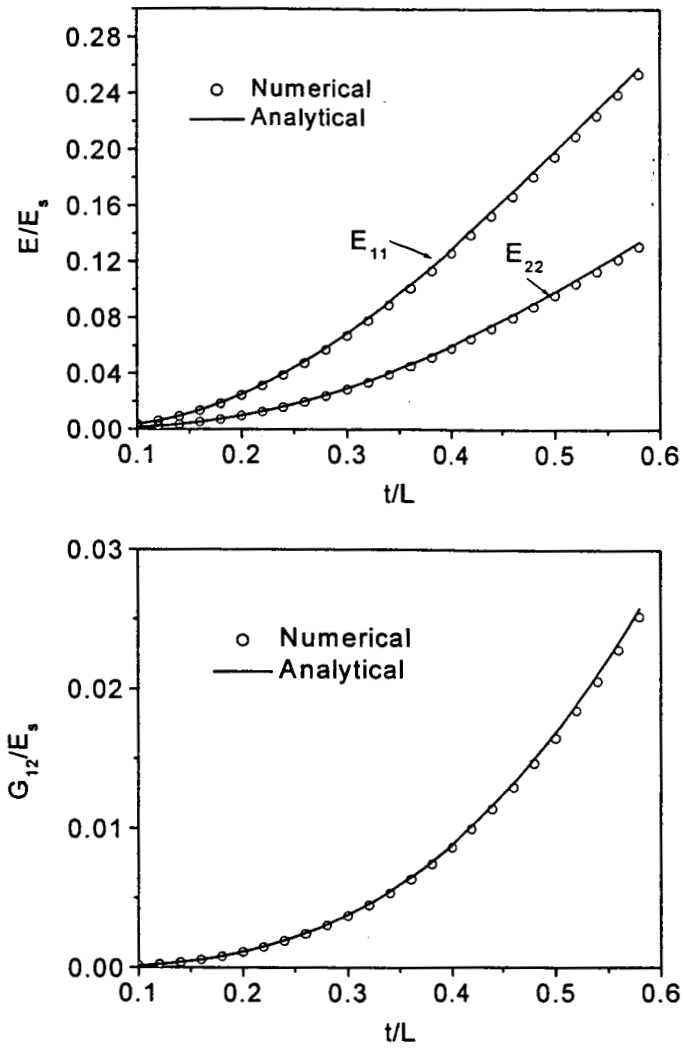


Figure 13. Comparison of elastic properties calculated numerically using 8*8*8 cells and the analytical results listed in Table 3.

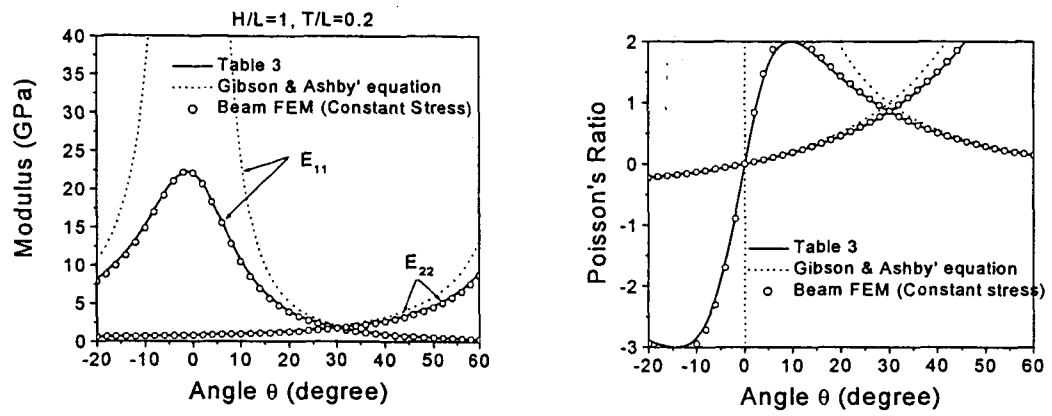


Figure 14. Comparison of elastic properties calculated using finite element beam method and analytical solutions for general hexagonal structure with different angles θ .

Compliances	C	B
S_{11}	$4L_zL_y$	0
S_{22}	$4L_zL_y$	0
S_{33}	$4L_xL_y$	0
S_{44}	0	$\frac{(4+\Phi_y)(L_y+L_z)L_xL_yL_z}{3}$
S_{55}	0	$\frac{(L_x\Phi_y + L_x\Phi_z + 4L_x + 4L_z)L_xL_yL_z}{3}$
S_{66}	0	$\frac{(4+\Phi_x)(L_x+L_y)L_xL_yL_z}{3}$

Table 4. Cell compliances for 3-D cubic structures.

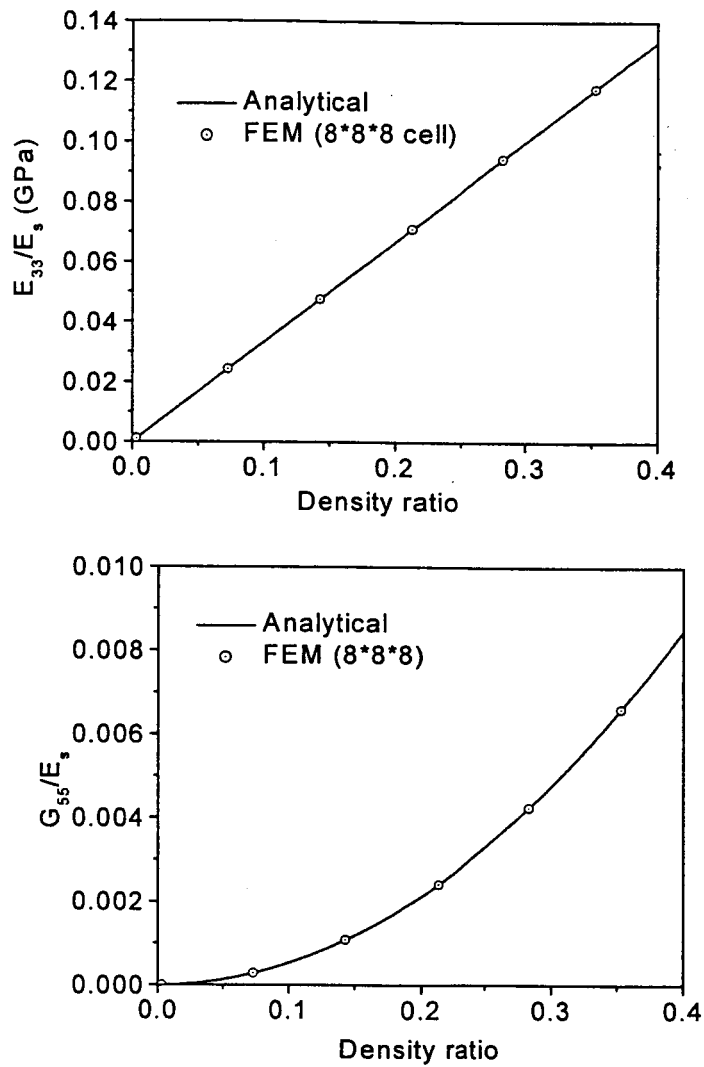
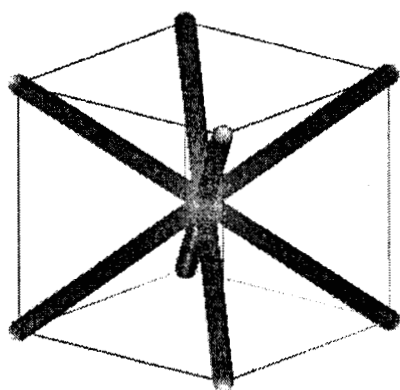
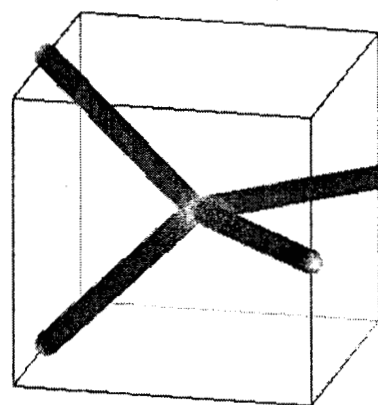


Figure 15. Comparison of elastic properties calculated numerically using 8*8*8 cells and the analytical results listed in Table 4.



(a)



(b)

Figure 16. The smallest repeating cells for (a) rhombic dodecahedron and (b) truncated octahedron shown in Figure 2.

Compliances	<i>C</i>	<i>B</i>
$S_{11} = S_{22}$	$\frac{\sqrt{3}L^2}{3}$	$\frac{\sqrt{3}L^4}{24}(3\Phi_x + \Phi_y + 16)$
S_{33}	$\frac{\sqrt{3}L^2}{3}$	$\frac{4L^4\sqrt{3}(\Phi_y + 4)}{9}$
S_{12}	$\frac{\sqrt{3}L^2}{3}$	$-\frac{L^4\sqrt{3}(3\Phi_x - \Phi_y + 8)}{24}$
$S_{13} = S_{23}$	$\frac{\sqrt{3}L^2}{3}$	$-\frac{L^4\sqrt{3}(\Phi_y + 4)}{12}$
$S_{44} = S_{55}$	0	$\frac{3\sqrt{3}L^4(16 + 3\Phi_x + \Phi_y)}{(AL^2(16 + 3\Phi_x + \Phi_y)/I + 8)}$
S_{66}	0	$\frac{3\sqrt{3}L^4(4 + \Phi_y)}{(AL^2(4 + \Phi_y)/I + 2)}$

Table 5. Cell compliances for rhombic dodecahedron structures.

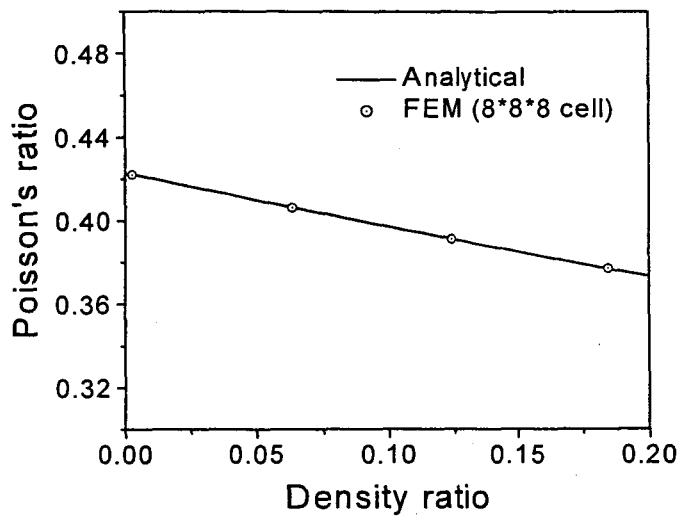
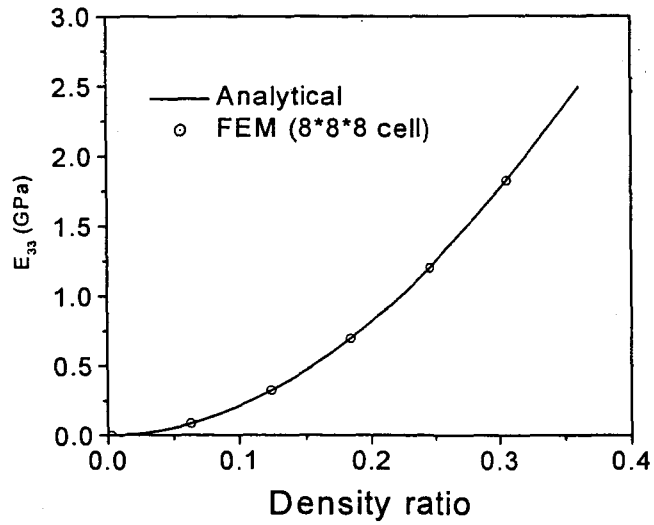


Figure 17. Comparison of elastic properties calculated numerically using 8*8*8 cells and the analytical results listed in Table 5.

Compliances	C	B
S_{11}	$\frac{8\sqrt{2}L^2}{3}$	$\frac{\sqrt{2}L^4}{9}(\Phi_x + \Phi_y + 8)$
$S_{22} = S_{33}$	$\frac{16L^2\sqrt{2}}{3}$	$\frac{4L^4\sqrt{2}(\Phi_x + 4)}{9}$
S_{12}	$\frac{8L^2\sqrt{2}}{3}$	$-\frac{2L^4\sqrt{2}(\Phi_x + 4)}{9}$
S_{13}	$\frac{8L^2\sqrt{2}}{3}$	$-\frac{2L^4\sqrt{2}(\Phi_y + 4)}{9}$
S_{44}	0	$\frac{8\sqrt{2}L^4}{9}(\Phi_x + \Phi_y + 8)$
S_{55}	$12L^2\sqrt{2}$	$\frac{\sqrt{2}L^4}{3}(\Phi_x + 4)$
S_{66}	$12L^2\sqrt{2}$	$\frac{\sqrt{2}L^4}{3}(\Phi_y + 4)$

Table 6. Cell compliances for truncated octahedron 3D structures.

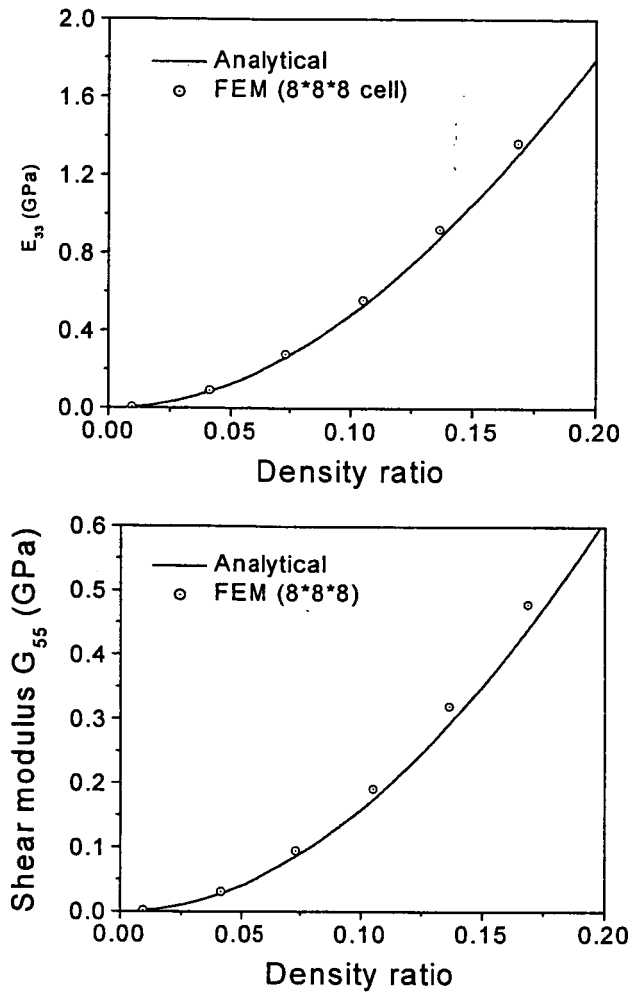


Figure 18. Comparison of elastic properties calculated numerically using 8*8*8 cells and the analytical results listed in Table 6.

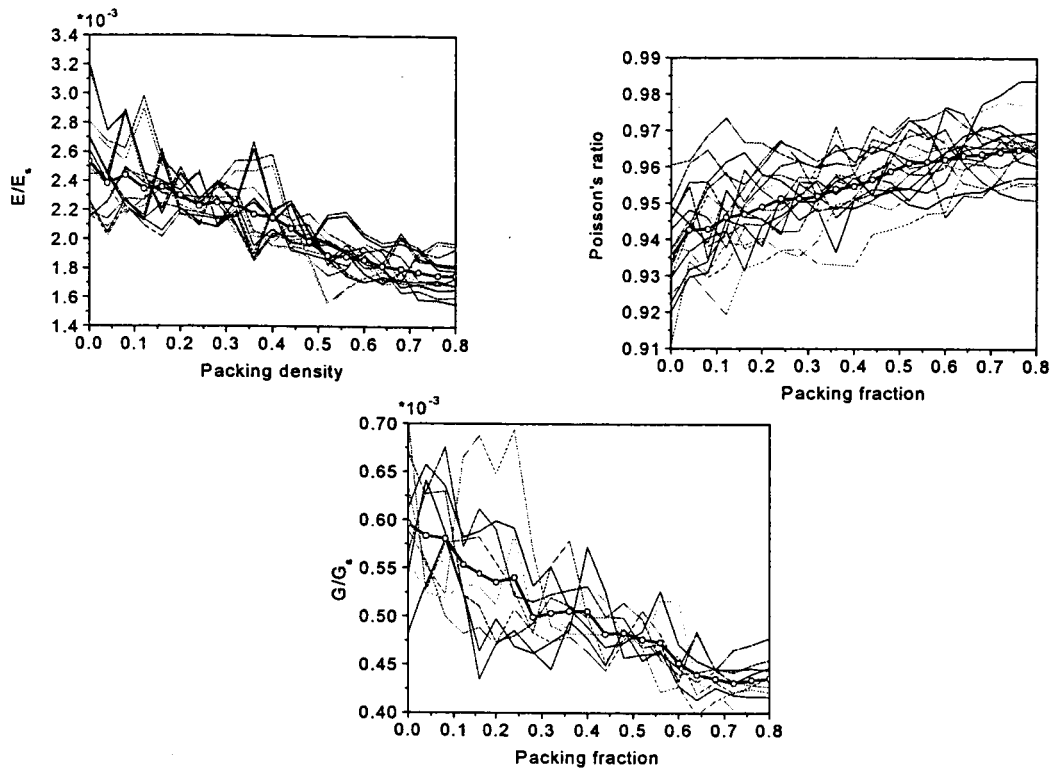


Figure 19. 2-D Elastic properties versus random packing fraction. 18 sets of random structures are calculated at each packing fractures. The thick line represents the average. The density ratio of the foam is 0.1.

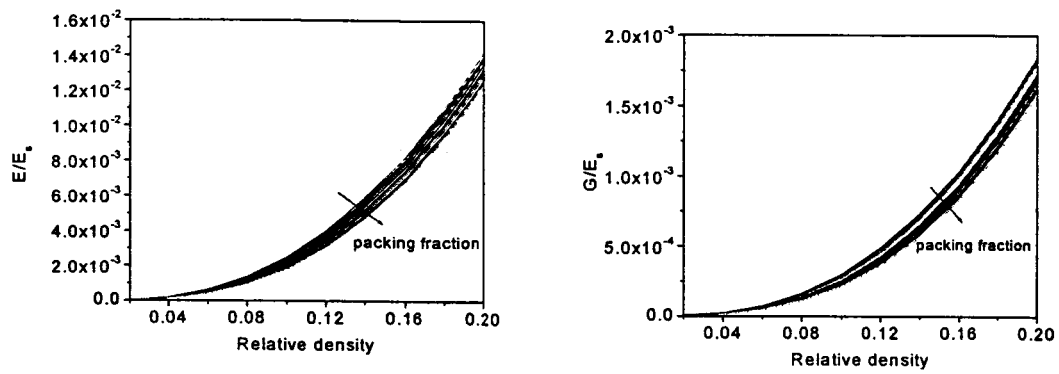


Figure 20. 2-D Elastic properties versus relative density for different packing fractions. 18 sets of random structures are calculated at each packing fraction.

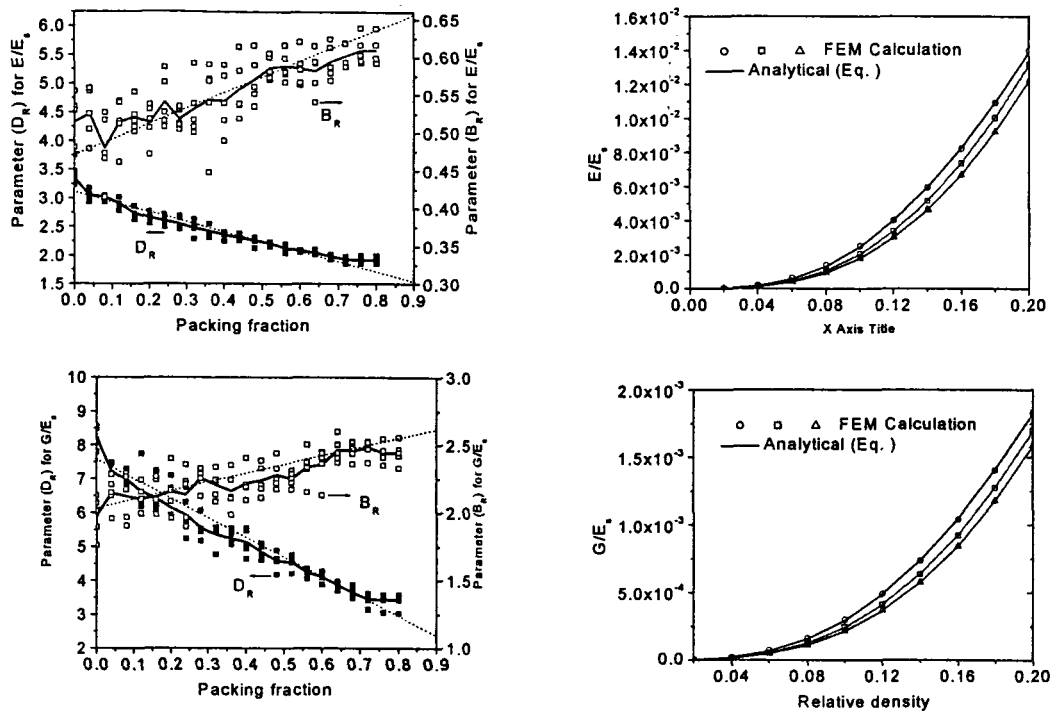


Figure 21. 2-D elastic properties versus random packing fraction. Nine sets of random structures are calculated at each packing fraction. The thick line represents the average. The density ratio of the foam is 0.1.

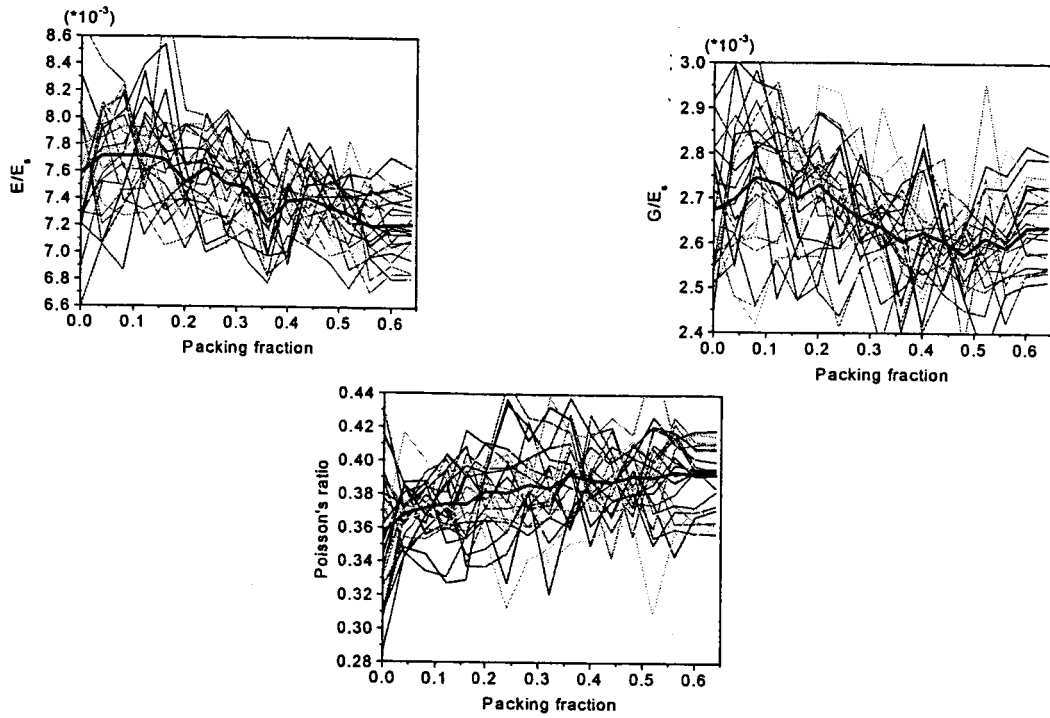


Figure 22. 3-D elastic properties versus random packing fraction. Nine sets of random structures are calculated at each packing fraction. The thick line represents the average. The density ratio of the foam is 0.1.